

Core-shell structure of LiMn_2O_4 cathode material reduces phase transition and Mn dissolution in Li-ion batteries

Chanikarn Tomon¹, Sangchai Sarawutanukul¹, Nutthaphon Phattharasupakun¹, Salatan Duangdangchote¹, Praeploy Chomkhuntod¹, Nattanon Joraleechanchai¹, Panyawee Bunyanidhi & Montree Sawangphruk¹✉

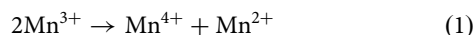
Although the LiMn_2O_4 cathode can provide high nominal cell voltage, high thermal stability, low toxicity, and good safety in Li-ion batteries, it still suffers from capacity fading caused by the combination of structural transformation and transition metal dissolution. Herein, a carbon-coated LiMn_2O_4 cathode with core@shell structure (LMO@C) was therefore produced using a mechanofusion method. The LMO@C exhibits higher cycling stability as compared to the pristine LiMn_2O_4 (P-LMO) due to its high conductivity reducing impedance growth and phase transition. The carbon shell can reduce direct contact between the electrolyte and the cathode reducing side reactions and Mn dissolution. Thus, the cylindrical cell of LMO@C//graphite provides higher capacity retention after 900 cycles at 1 C. The amount of dissolved Mn for the LMO@C is almost 2 times lower than that of the P-LMO after 200 cycles. Moreover, the LMO@C shows smaller change in lattice parameter or phase transition than P-LMO, indicating to the suppression of $\lambda\text{-MnO}_2$ phase from the mixed phase of $\text{Li}_{1-\delta}\text{Mn}_2\text{O}_4 + \lambda\text{-MnO}_2$ when Li-delithiation at highly charged state leading to an improved cycling reversibility. This work provides both fundamental understanding and manufacturing scale demonstration for practical 18650 Li-ion batteries.

¹Center of Excellence for Energy Storage Technology (CEST), Department of Chemical and Biomolecular Engineering, School of Energy Science and Engineering, Vidyasirimedhi Institute of Science and Technology, 555 Moo 1 Payupnai, Wangchan District, Rayong 21210, Thailand.

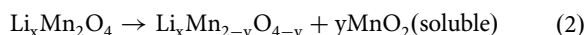
✉email: montree.s@vistec.ac.th

Nowadays, rechargeable Li-ion batteries (LIBs) have become essential energy storage devices due to their high energy densities suitable for many electronic devices such as mobile phones and electric vehicles (EVs). The performance of LIBs is mainly determined by the cathode materials, which share ca. 30% of the total cost of LIB materials¹. Thus, many extensive publications^{2–5} have been studied to develop effective cathode materials trying to increase energy and power densities and improve its stability, which are the important factors for the industrial production scale of LIBs. The face-centered cubic (fcc) spinel of LiMn₂O₄ (LMO) has received widespread attention due to its three-dimensional (3D) structure⁶, which can improve ion transport and power capability especially at high rates⁷. Moreover, LMO provides higher nominal voltage (ca. 4.0 V)⁸ than LiCoO₂ (ca. 3.6 V)⁹, high thermal stability, low toxicity, and good safety which can simply be applied for large-scale energy storage applications^{10,11}. However, the LMO is suffered from capacity fading caused by the combination of structural transformation and transition metal dissolution¹². The Jahn–Teller distortion, occurred at the discharge state, introduces the structural change from cubic LiMn₂O₄ to tetragonal Li₂Mn₂O₄ which causes the large anisotropic volume change (16%) as well as the structural damage^{13,14}. To suppress the Jahn–Teller effect, Xiaohui Zhu et al.¹⁵ presented a unique heterostructure design consisting of layered and spinel domains, disrupting the long-range Jahn–Teller ordering. As a result, they can enhance structural and electrochemical cycling stability.

Apart from Jahn–Teller effect, the Mn dissolution is one of the most important issues. The Mn dissolution from the spinel LiMn₂O₄ occurs in various situations such as at the aqueous acid solution, the high charging state, HF attack, and the over discharge state¹⁶. The main dissolution mechanism comes from the disproportionation reaction of Mn³⁺ to Mn⁴⁺ and Mn²⁺ as shown in [Eq. 1].



In the overcharging process with Mn⁴⁺-rich state, the increasing Mn dissolution was caused by the instability of the delithiated structure at the end of the charging leading to loss of MnO to form a more stable single-phase structure. The phase transformation can cause the Mn dissolution from the spinel at the high potential as simply described in [Eq. 2]^{16,17}.



After the Mn dissolution, the MnO (Mn²⁺) then dissolves into the electrolyte and migrates to the anode driven by the concentration gradient and/or electric field force and thereby deposits on the graphite surface so-called DMD process described in the [Eq. 3]¹⁸;



The Mn⁰ gradually covers the anode surface, interfering with the lithium intercalation into the graphite and also increases the anode impedance¹⁶. Moreover, Delacourt et al.¹⁹ proposed that the deposited Mn can react with carbonate and Li⁺ in the electrolyte forming the inactive LiCO₃. This process consumes active Li ions over extended cycles, thus leading to severe capacity fading^{12,20}.

The occurrence of Mn dissolution not only from the disproportionation reaction but also from HF attack from LiPF₆ decomposition reacts with trace amount of water²¹. In addition, the capacity fading of the LMO cathode is deteriorated from the contraction/expansion of the crystal lattice during phase transition and also the generation of λ-MnO₂ phase during charging process²².

Various strategies have been studied to develop the LMO material such as the synthesis of nanomaterials^{23,24}, ion

doping^{25–27}, and surface coating^{28–30}. Nonetheless, the doping and synthesis of nanomaterials lead to the reduction of overall cell capacity due to the electrochemically inactive cation dopants^{31,32} and the poor packing density of nano-grains^{33,34}, respectively. Moreover, they cannot prevent the Mn dissolution from side reactions occurring at the interface between the electrode and the electrolyte during the charge/discharge processes. On the other hand, the surface coating can minimize the direct contact between the active cathode and the electrolyte, reduce Mn dissolution, and alleviate the Mn deposition on the anode surface resulting in less impedance growth^{35–37}. However, the surface engineering/coating normally requires complex synthesis processes and high cost, for example, wet chemical coating and atomic layer deposition which will be ineffective for uses in commercial-scale LIBs.

Recently, a surface coating as the core-shell morphology using a simple and solvent-free mechanofusion process has been proposed as an efficient method for the development of cathode materials for scalable LIBs^{37,38}. Specifically, carbon coating has received much attention because carbon can facilitate the continuous electron pathway through the coated shell leading to an improved active material utilization^{39,40}. Moreover, some previous publications show that the carbon coating can improve the stability and reduce the Mn dissolution⁴⁰. Nevertheless, the fundamental understanding on the minimized phase transformation from the carbon-coated LMO core-shell has not yet been investigated. In this work, the mechano-thermal carbon-coated LMO core-shell can suppress the phase transformation, especially reducing the occurrence of an unstable two-phase region (Li_{1-δ}Mn₂O₄ + λ-MnO₂ mixed phase) at high potential.

Herein, the nano-sized conductive carbon coated on the LMO (LMO@C) cathode was synthesized using a dry mechanofusion technique. After the coating process, the 18650 cylindrical LIBs of LMO@C cathode coupled with graphite anode were fabricated in a dry room. The LMO@C exhibits superior cycling stability compared with pristine-LMO (P-LMO), which can mainly attribute to the reduction of Mn dissolution-migration-deposition (DMD) process as investigated by the post-mortem analyses using ex situ SEM/EDS, ICP-OES, and ex situ XPS techniques. In addition, the structural transformation is explored by *in operando* X-ray diffraction (XRD) during charging and discharging. The *in situ* XRD of P-LMO reveals the rapid drop in lattice parameter (a/Å) when Li deintercalated over ca. 70%, indicates to the generation of λ-MnO₂ phase mixed with Li_{1-δ}Mn₂O₄²². However, the LMO@C exhibits lower change in lattice parameter implying to the lower generation of λ-MnO₂ in Li_{1-δ}Mn₂O₄ + λ-MnO₂ mixed phase. These results confirm that the carbon shell can minimize Mn dissolution and stabilize phase transformation, which will be beneficial for improving the battery lifetime.

Results and discussion

Physicochemical properties. The morphologies of pristine-LMO (P-LMO), carbon black, and LMO@carbon core@shell (LMO@C) materials synthesized by the mechanofusion process were investigated by FE-SEM/EDS, HRTEM, and STEM-EDS as shown in Fig. 1. From Fig. 1a, the P-LMO shows the secondary particle consisting of primary particles with the octahedral structure. Figure 1b shows the morphology of carbon nanospheres with individual particle size of ca. 50 nm. After the mechanofusion of P-LMO with carbon nanoparticles, the applied high compression and shear forces can fuse the carbon nanoparticles into the surface of LMO providing the core-shell like structure with the diameter of ca. 8 μm (Fig. 1c)^{37,41}. EDX and STEM-EDS results (Fig. 1d–h) confirm the uniform carbon coating in which the atomic ratio of C at the shell decreases to 0% when approaching

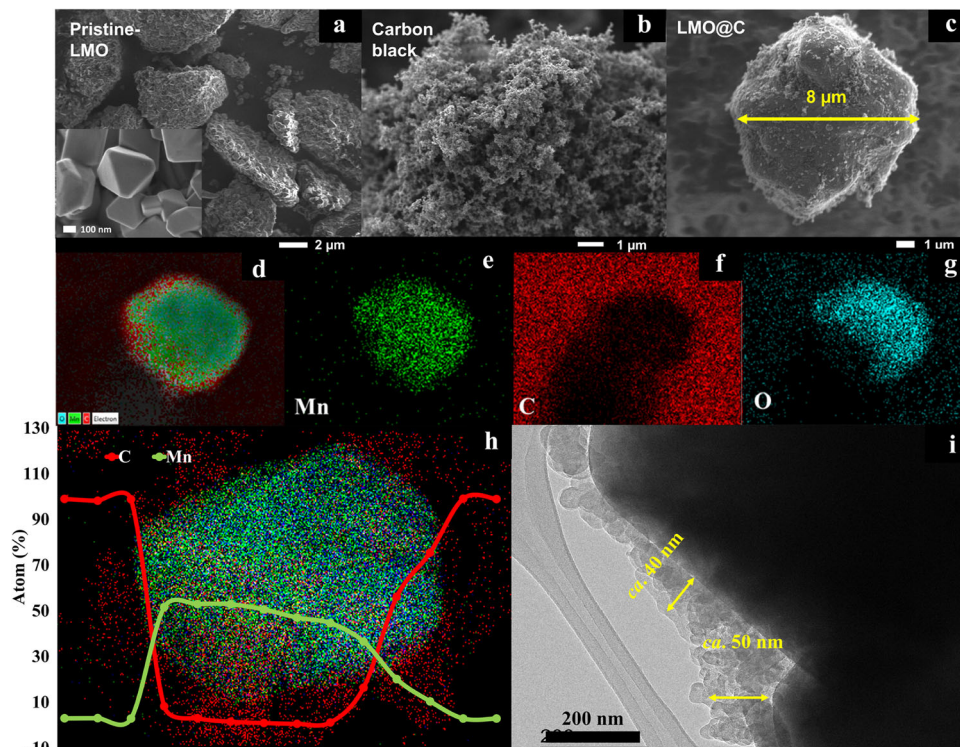
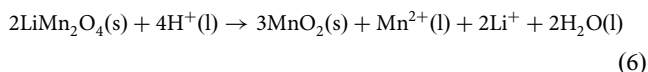
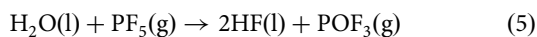
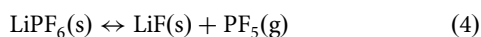


Fig. 1 Morphology of pristine-LMO and LMO@C materials. SEM images of (a) pristine-LMO, (b) carbon black, and (c) LMO@C. d-g SEM-EDS of LMO@C. h STEM-EDS line scanning of LMO@C. i HR-TEM images of LMO@C.

to the center of LMO@C particle. In contrast, the percentage of Mn atom increased when approaching to the center of the particle. The HRTEM image (Fig. 1i) shows the carbon shell thickness of *ca.* 40–50 nm composing of 2–4 overlapping carbon nanospheres with no void spaces at the interface between the core particles and carbon shells. The effective adherence of carbon and LMO can be attributed to the strong compressive force and high heat energy generated during the mechano-thermal process^{42,43}. The carbon coating layer is expected to improve electrical conductivity of the material and suppress the Mn dissolution as it can prevent the direct contact from the electrolyte and prohibit the acute HF attack. Note, HF is generated from the decomposition of LiPF₆ as shown in [Eq. 4–6]²¹.



Moreover, the Mn dissolution can occur from the instability of the delithiated structure at high SOC leading to the loss of MnO and forming λ -MnO₂ as shown in [Eq. 1]⁴⁴.

The structure of P-LMO and LMO@C were investigated using XRD as shown in Fig. S1a. The XRD patterns of P-LMO and LMO@C can be well indexed to the cubic spinel phase of *Fd(-)3m* space group (JCPDS 98-005-0256), corresponding to (111), (311), (222), (400), (331), (511), (440), and (531) planes. In this structure, lithium, manganese, and oxygen reside on the 8a (tetrahedral sites), 16d (octahedral sites), and 32e Wyckoff sites, respectively⁴⁵. No obvious peaks from carbon coating could be observed by XRD, due to its small quantity as well as its amorphous characteristic^{40,46}. However, in the inset image of Fig. S1a, the slight peak shift toward higher 2Theta corresponded to the compression effect during the mechano-fusion process^{47,48}. To gather detailed information of the

structure, Rietveld refinement was performed using the Rietica software. The refinement data are presented in Fig. S2 and Table S1, respectively. The similar lattice parameters of 8.233 Å in both P-LMO and LMO@C indicated that the carbon coating does not alter the unit cell structure of the active material.

Figure S1b shows the Raman spectra of P-LMO and LMO@C. Normally, LMO with *Fd(-)3m* space group has five Raman-active modes represented by the species of A_{1g} + E_g + 3F_{2g}^{49,50}. Both of P-LMO and LMO@C present a dominant peak at 630 cm⁻¹ relating to Mn-O vibrational mode in the MnO₆ octahedral. Moreover, two bands located at *ca.* 492 and 585 cm⁻¹ refer to high-frequency scattering bands of F_{2g}(2) and F_{2g}(3) that result from the large and small Mn atom vibrations, respectively^{49,51,52}. The E_g band located at 382 cm⁻¹ also corresponds to the O vibration⁵³. It can be noticed that there is no obvious peak shift after the mechano-fusion of carbon coating process. Thus, the mechano-fusion process did not change the characteristics of LMO. However, the two distinct peaks in LMO@C were founded at 1360 and 1592 cm⁻¹, corresponding to the A_{1g} and E_{2g} vibrational modes of the disorder (D) and graphitic (G) bands, which are the typical peaks of carbon. A broad peak at 2701 cm⁻¹ indicates the 2D band of carbon^{40,54}. The appearance of I_D, I_G, and 2D bands only in LMO@C indicates to the carbon content from the carbon coated on LMO@C.

The TGA of P-LMO and LMO@C was used to investigate the amount of carbon shell coated on the LMO core as shown in Fig. S1c. The TGA profile of P-LMO shows a slightly weight loss with only 1.58 wt.% during the whole temperature measurement. Conversely, the LMO@C exhibits the mass loss from residual moisture and other volatiles with *ca.* 2.4 wt.% before 400 °C, and then rapidly drop of *ca.* 10 wt.% at 400 °C according to the oxidation of carbon at the shell³⁷.

The elemental composition and the oxidation state of P-LMO and LMO@C were further characterized by the XPS technique as shown in Fig. S1d and Fig. 2. In wide-scan XPS spectra, the sharp

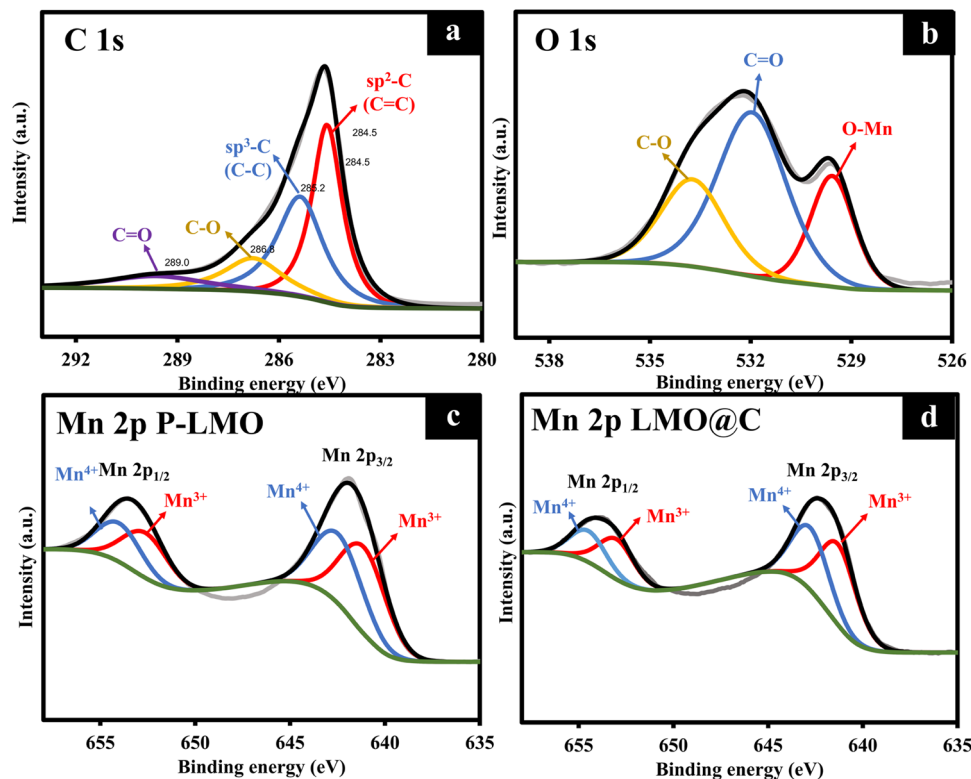
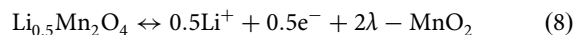
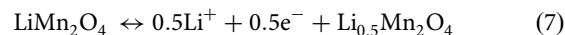


Fig. 2 The elemental composition and the oxidation state of P-LMO and LMO@C. **a-d** Narrow-scan XPS spectra of (a) C 1s of LMO@C, (b) O 1s of LMO@C, (c) Mn 2p of P-LMO, and (d) Mn 2p of LMO@C.

peaks of C 1s, O 1s, and Mn 2p are located at *ca.* 245, 532, and 642 as well as 654 eV, respectively. The C 1s intensity in LMO@C is significantly higher than P-LMO due to the existence of carbon shell. The peak deconvolution and fitting of narrow scans (Fig. 2) were carried out using Gaussian–Lorentzian shaped peaks based on the Shirley background correction. The C1s spectrum of LMO@C (Fig. 2a) displays four deconvoluted peaks comprising of sp^2 -C, sp^3 -C, C–O, and C=O located at 284.5, 285.2, 286.8, and 289.0 eV, respectively^{55,56}. The O 1s spectrum of LMO@C (Fig. 2b) shows three main components at 529.3, 531.8, and 533.4 eV correlating to O^{2-} anions of $LiMn_2O_4$ ⁵⁷, C=O, and C–O–C (surface adsorbed species), respectively^{55,58,59}. Two typical peaks corresponding to a spin–orbit splitting of Mn $2p_{3/2}$ and $2p_{1/2}$ are observed in the P-LMO (Fig. 2c) and LMO@C spectra (Fig. 2d)⁶⁰. Both of them present similar splitting binding energy about 11.6 eV agreeable well with the previous reports^{40,61}. The deconvoluted Mn 2p of P-LMO displays the mixing of Mn^{3+} and Mn^{4+} for which the binding energies of Mn^{3+} are 641.2 eV ($2p_{3/2}$) and 652.7 eV ($2p_{1/2}$), whereas those of Mn^{4+} are 642.6 eV ($2p_{3/2}$) and 654.2 eV ($2p_{1/2}$). For the LMO@C, the binding energies of Mn^{3+} are 641.3 eV ($2p_{3/2}$) and 652.9 eV ($2p_{1/2}$) and those of Mn^{4+} are 642.7 eV ($2p_{3/2}$) and 654.5 eV ($2p_{1/2}$). The ratios of Mn^{3+}/Mn^{4+} of P-LMO and LMO@C are 1.17: 1 and 1.07:1, respectively. The Mn^{3+}/Mn^{4+} ratio of LMO@C is lower than that of P-LMO and also close to an expected theoretical ratio of 1:1. In principle, the electrochemically active Mn^{3+} is not stable so the higher ratio in the structure can lead to the Mn^{3+} disproportionation^{40,55}. According to these results, the carbon coating may be able to reduce the Mn dissolution.

Electrochemical property of coin-cell batteries. The electrochemical tests were firstly performed in the half-cell configurations of Li//P-LMO and Li//LMO@C. These results are shown in Fig. 3. According to charge/discharge profiles (Fig. 3a, b) over the

voltage range of 3.0–4.3 V vs. Li/Li⁺, both P-LMO and LMO@C provide two distinct plateaus at around 4.0 and 4.15 V vs. Li/Li⁺. These corresponds to the two reversible deintercalation/intercalation reactions of Li⁺ from the tetrahedral sites in the dQ/dV results (Fig. 3c), described in Eqs. 7 and 8^{62,63}.



During the charging process, half of the Li⁺ ions are deintercalated from the tetrahedral sites in $LiMn_2O_4$ (Eq. 7) and associated with the first plateau at *ca.* 4.0 V vs. Li/Li⁺. After that, further de-lithiation continuously occurs to form the final product with λ - MnO_2 (Eq. 8) that can be indexed to the second plateau at *ca.* 4.15 V vs. Li/Li⁺⁶⁴.

According to Fig. 3c, the peak potential difference (ΔE_p) between the oxidation and the reduction can suggest the polarization degree of the battery⁶⁵. The lower ΔE_p values of LMO@C (20 mV) than P-LMO (40 mV) indicate that LMO@C has a smaller electrochemical reaction polarization than P-LMO. Moreover, the rate performance and profiles at different C-rates for P-LMO and LMO@C are shown in Fig. 3d. The discharge capacities of LMO@C are about 129.6, 115.7, 107.1, 93.7, and 82.3 mAh g⁻¹ obtained from 0.1 C, 0.5 C, 1 C, 2 C, and 3 C, respectively. On the other hand, P-LMO exhibits the specific discharge capacities of 121.3, 107.3, 96.7, 84.1, and 66.3, and 48.0 mAh g⁻¹ corresponding to 0.1 C, 0.5 C, 1 C, 2 C, and 3 C, respectively. The low specific capacities at high C-rate are attributed to the increasing electrode polarization, attributed from the increasing overpotential and the increasing internal resistance or IR drop⁶⁶. As compared with the P-LMO, the LMO@C shows lower polarization and higher capacity at high C-rates which could be ascribed to the improved electron conductivity, thereby increasing the active material utilization⁴⁰.

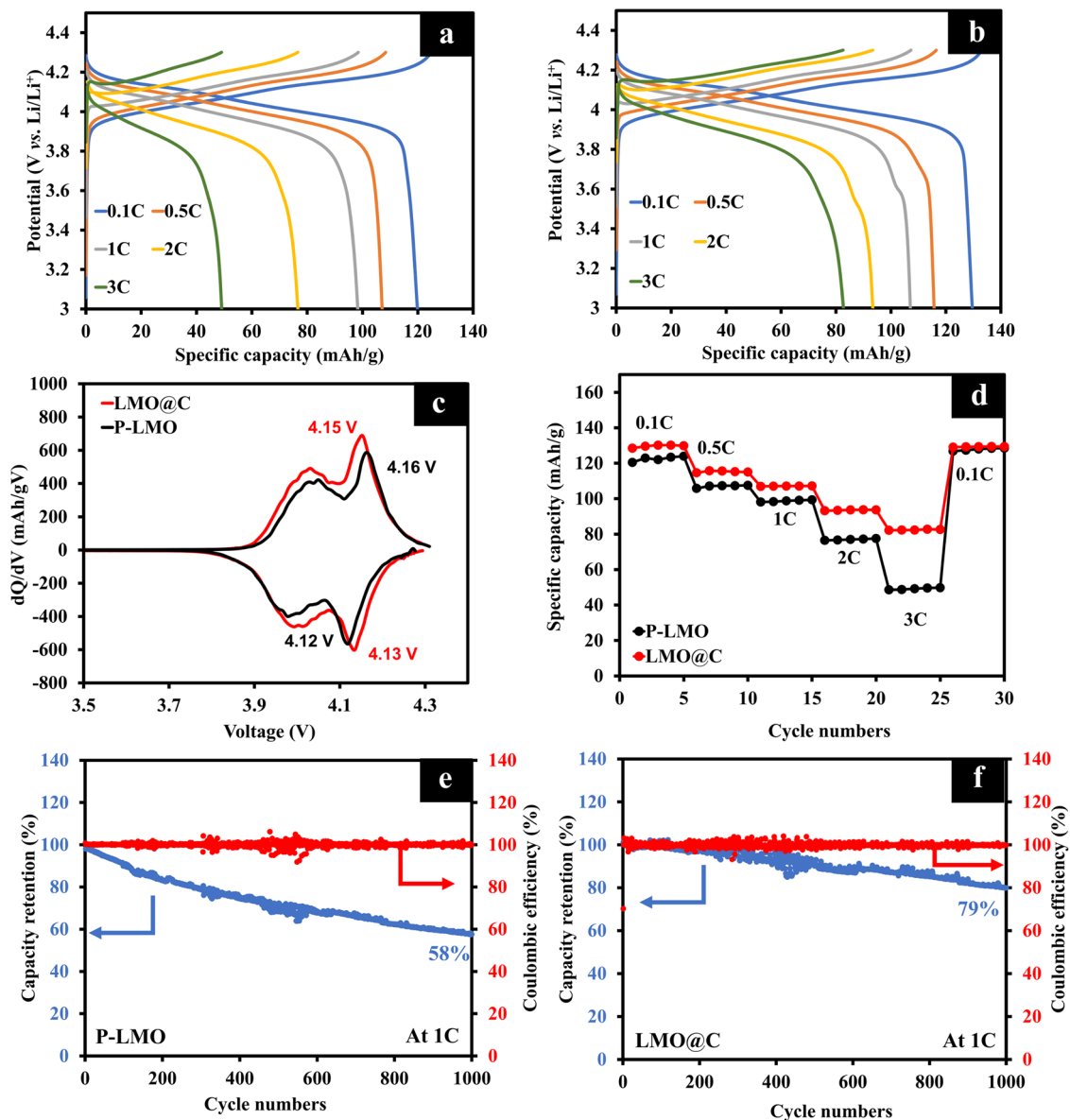


Fig. 3 Electrochemical performance of half-cell configurations for Li//P-LMO and Li//LMO@C. **a–b** Galvanostatic charge/discharge curves at different C-rates of **(a)** P-LMO and **(b)** LMO@C. **c** The dQ/dV curves of P-LMO and LMO@C. **d** The rate capability of P-LMO and LMO@C. **e–f** The cycling stability test of **(e)** P-LMO, and **(f)** LMO@C at 1C.

Furthermore, the long-term cycling test was carried out to confirm the improved electrochemical property of LMO@C compared with P-LMO at 1C (Fig. 3e, f). Obviously, the LMO@C provides superior capacity retention of 79% after 1000 cycles which is considerably higher than that of the P-LMO (58% capacity retention). The coulombic efficiency is maintained around 99% for the 1000 cycles for both LMO@C and P-LMO. The enhanced cycling stability from the carbon coating could be explained by (i) less direct contact between the electrode and the electrolyte, (ii) suppression of Mn dissolution, migration into an electrolyte, and deposition at anode surface so-called “DMD process” which will be further investigated by ex situ SEM, ICP-OES, and XPS in the next sections, (iii) increasing of phase stabilization that will be examined by in situ XRD, and (iv) the improved conductivity^{67–69}.

Electrochemical properties of cylindrical 18650 cells. To demonstrate the practical application and scalable process of

LMO@C, the 18650 cylindrical LIBs were fabricated in a dry room with dew point temperature of -40°C for all production units except for the electrolyte injection unit at -55°C . The P-LMO cylindrical LIBs were assembled for comparison. Both LMO@C and P-LMO were coupled with graphite anode and with a commercial LMO electrolyte (EC+DMC+DEC). Fig. S3 illustrates the diagrams and photographs of the 18650 LIBs manufacturing process. The four-point probe measurements (Table S2) were also carried out to measure the resistance of each electrode. Interestingly, LMO@C cathode provides a resistivity just only $0.47\text{ m}\Omega/\text{cm}$ which is five times lower than P-LMO cathode. This indicates that the carbon shell can dramatically increase conductivity of the electrode^{70–72}.

To determine the electrochemical performances (Fig. 4), the LMO@C/graphite and P-LMO/graphite cells were tested in a voltage range of 3.0–4.2 V at 0.1C (Fig. 4a) by using CC-CV charging method. The results show the same capacity of around 1277 mAh/cell in LMO@C as well as P-LMO with the nominal voltage of 3.93 V. Whilst, the rate-capability (Fig. 4b) of

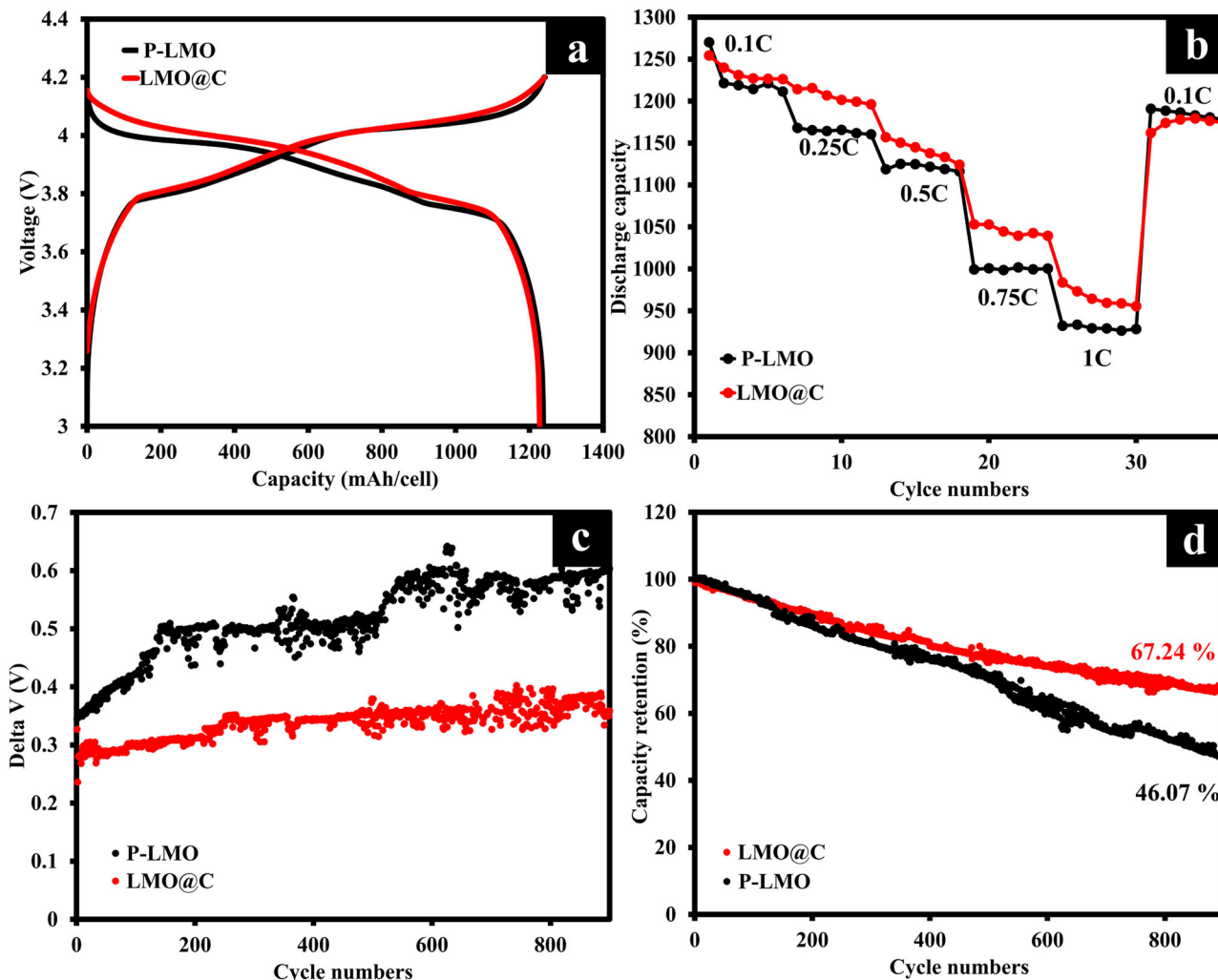


Fig. 4 Electrochemical performances of cylindrical 18650 P-LMO//graphite and LMO@C//graphite cells. **a** Galvanostatic charge/discharge profiles of P-LMO and LMO@C cells. **b** Rate-capability of P-LMO and LMO@C cells. **c** Delta V vs. cycle of P-LMO and LMO@C cells. **d** Cycling stabilities of P-LMO and LMO@C cells.

LMO@C//graphite is slightly better at the high rates of 0.75 C and 1 C which could be attributed to the enhanced conductivity from carbon coating as discussed in previous section.

Figure 4c shows the difference between average charge and discharge voltage (ΔV) vs. cycle numbers for P-LMO//graphite and LMO@C//graphite cells. The ΔV values during cycling can describe the impedance growth and polarization in the cells^{73,74}. The P-LMO//graphite cell exhibits significant increase in ΔV during cycling, indicating an impedance increase. In contrast, the LMO@C//graphite cell shows smaller ΔV due to the smaller polarization in the cell and lower impedance compared with P-LMO//graphite.

Figure S4a and S4b present the dQ/dV over 100 cycles at 0.1 C for P-LMO and LMO@C, respectively. Both provide two distinct oxidation-reduction peaks located at *ca.* 4.07/3.94 and 3.74/3.83 V, indicating to the reversible deintercalation/intercalation of Li^+ from the tetrahedral sites as mentioned in Eqs. 7 and 8. The peak potential difference (ΔE_p) values of 1st and 100th cycles of P-LMO are 80.6 and 137 mV, respectively. Whilst the LMO@C shows lower peak potential different at 100th cycle (98 mV) compared to the 1st cycle (80.7 mV). This indicates that the LMO@C exhibits better reversibility than the P-LMO⁷⁵.

The constant current stability test was carried out at a high rate of 1 C for 900 cycles as shown in Fig. 4d. The capacity retention of

P-LMO//graphite cell dramatically decreased to 46% at 900 cycles, that could be attributed to the Mn dissolution, the Mn redeposition at anode site, mixed phase transition, and poor conductivity. In contrast, the LMO@C can maintain the capacity retention at 67.24% after 900 cycles, suggesting that carbon shell can improve the stability of cylindrical LIBs.

Post-mortem analysis. The post-mortem analyses including ex situ SEM, ex situ XPS, ex situ ICP-OES, and in situ XRD were carried out to investigate the origin of capacity fading. In principle, the DMD process has been generally accepted that it is the crucial factor giving rise to the capacity fade of Mn-based LIBs¹⁶. Figure S5 presents the ex situ SEM images and EDS mapping of graphite anode disassembled from the P-LMO//graphite (Fig. S5a) and LMO@C//graphite (Fig. S5b) after 200 cycles. According to Fig. S5, the % Mn content on graphite from P-LMO (2%) is approximately two times higher than graphite from LMO@C (1.1%), indicating to the reduction of DMD process in LMO@C. Moreover, the results from the ICP-OES measurement reveal the amount of Mn deposition on the graphite surface after 200 cycles. According to Table S3, the concentration of Mn deposited on anode side of P-LMO//graphite, and LMO@C//graphite cells were 0.022 mg/l and 0.01 mg/l, respectively. These results agree well with ex situ SEM and EDS mapping.

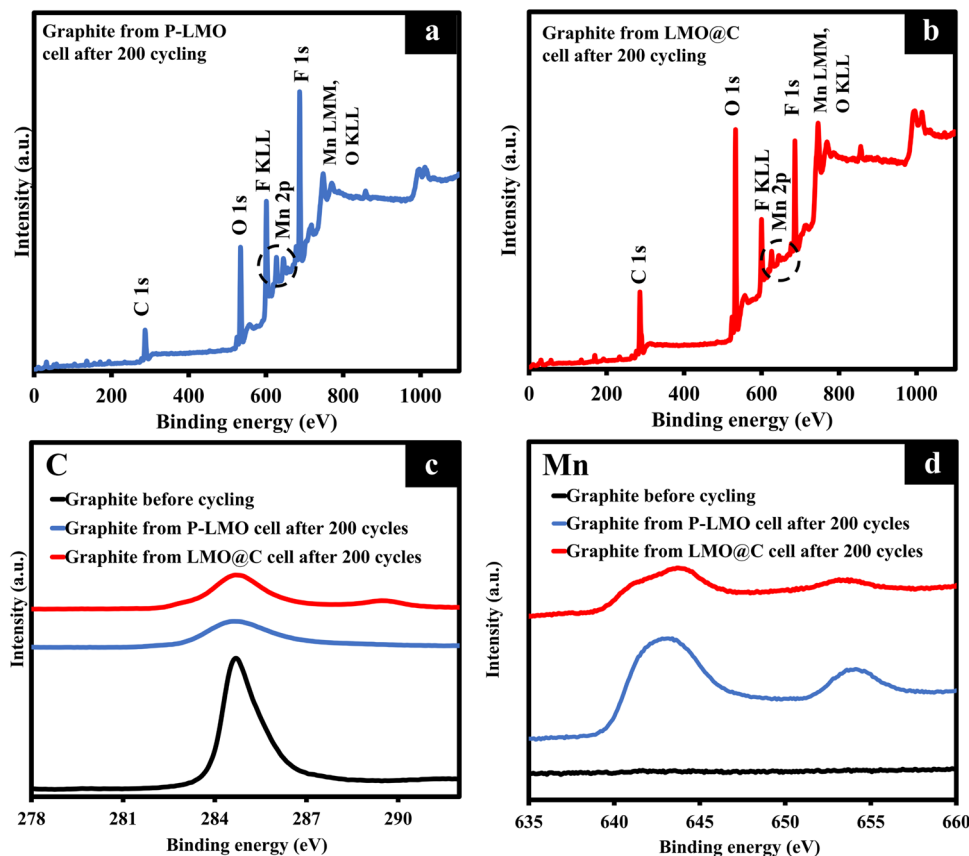
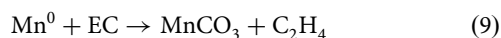


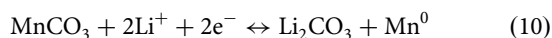
Fig. 5 Ex situ XPS of cathodes disassembled from P-LMO//graphite and LMO@C//graphite cells after cycling. **a–b** Wide-scan XPS of (a) P-LMO electrode, and (b) LMO@C electrode. **c–d** Narrow-scan XPS of (c) C 1s orbitals, and (d) Mn 2p orbital of controlled graphite (before cycling), disassembled graphite from P-LMO//graphite and LMO@C//graphite cells after 200 cycles.

The surface analysis by the ex situ XPS (Fig. 5 and Table S4) of graphite anodes after cycling were revealed as the strong evidence for the occurrence of DMD process. Figure 5a, b show the wide-scan spectra from graphite anodes disassembled from P-LMO//graphite and LMO@C//graphite, respectively. These two anodes show the main compositions of C, O, Mn, and F, in which F came from the decomposition of LiPF_6 or SEI layer⁷⁶. Furthermore, Fig. 5d displays the narrow scan Mn 2p spectra on graphite surfaces before and after cycling for which the cycled P-LMO//graphite and LMO@C//graphite disassembled for XPS measurement. After cycling, the Mn was detected in both anodes from the cycled P-LMO and LMO@C cells, but the Mn intensity from the cycled P-LMO cell is significantly higher than that of the cycled LMO@C cell. The Mn/C ratios of anodes from the cycled P-LMO and LMO@C are 0.25 and 0.17 (Table S4), respectively. Therefore, this clearly indicated that the carbon coating can suppress the Mn dissolution.

Note that the observed Mn peaks situated around 641 eV indicate manganese divalent or trivalent such as MnO and Mn_2O_3 ⁷⁷. These results suggest the irreversible decomposition and thick deposition by Mn (II) dissolution⁷⁷. After the Mn (II) dissolution [Eq. 2], metallic Mn was first deposited on the anode surface and subsequently reacts with organic species in electrolyte as shown in [Eqs. 9 and 10]^{18,19,78,79}.



A conversion reaction could occur between MnCO_3 and Li^+ as follows:



The [Eq. 10] occurs reversibly during cycling and changes the morphology of the SEI continuously, resulting in the occurrence of cracks and pores in SEI layer¹⁹. Moreover, the Mn ions dissolve or strip from the cathode and redeposit or plate on the anode surface, which can block Li^+ diffusion pathways leading to the increasing impedance⁸⁰. These two reasons can directly affect the capacity fading of the practical cell.

In operando XRD. The structural transition of P-LMO and LMO@C cathodes upon lithium deintercalation/intercalation was investigated by *in operando* XRD as shown in Fig. 6. *In operando* XRD of P-LMO (Fig. S6) and LMO@C (Fig. 6a) cathodes show two-phase transition stages during charge/discharge process relating to two peaks observed in its dQ/dV curves. In the first charging state with less than 50% Li extraction, the XRD peaks gradually shifted to higher 2Theta (Fig. S6 and Fig. 6a) according to the decrease in lattice parameters (Fig. 6b, c). The increasing in the average Mn oxidation state led to the decrease in ionic radius and cell dimensions^{81–83}. In the following region, when Li extraction exceeds 50% (ca. 4.05 V), further de-intercalation of Li^+ ion from the $\text{Li}_{0.5}\text{Mn}_2\text{O}_4$ induces a solid-solution reaction to form Li-deficient $\text{Li}_{1-\delta}\text{Mn}_2\text{O}_4$ ^{12,22}. Furthermore, at high state of charge (SOC), the mixed phase of $\text{Li}_{1-\delta}\text{Mn}_2\text{O}_4$ and $\lambda\text{-MnO}_2$ was formed, which can be noticed by the occurring of new phase at the end of charge (red circle) in Fig. 6a and Fig. S6. After Li re-intercalation (discharge process), the XRD peaks shifted back to lower 2Theta, indicating the existence of reversible phase transformation to cubic LiMn_2O_4 ⁸¹.

From previous reports^{62,81,82,84}, there are three phases in the phase transition including a single-phase LiMn_2O_4 , the mixed

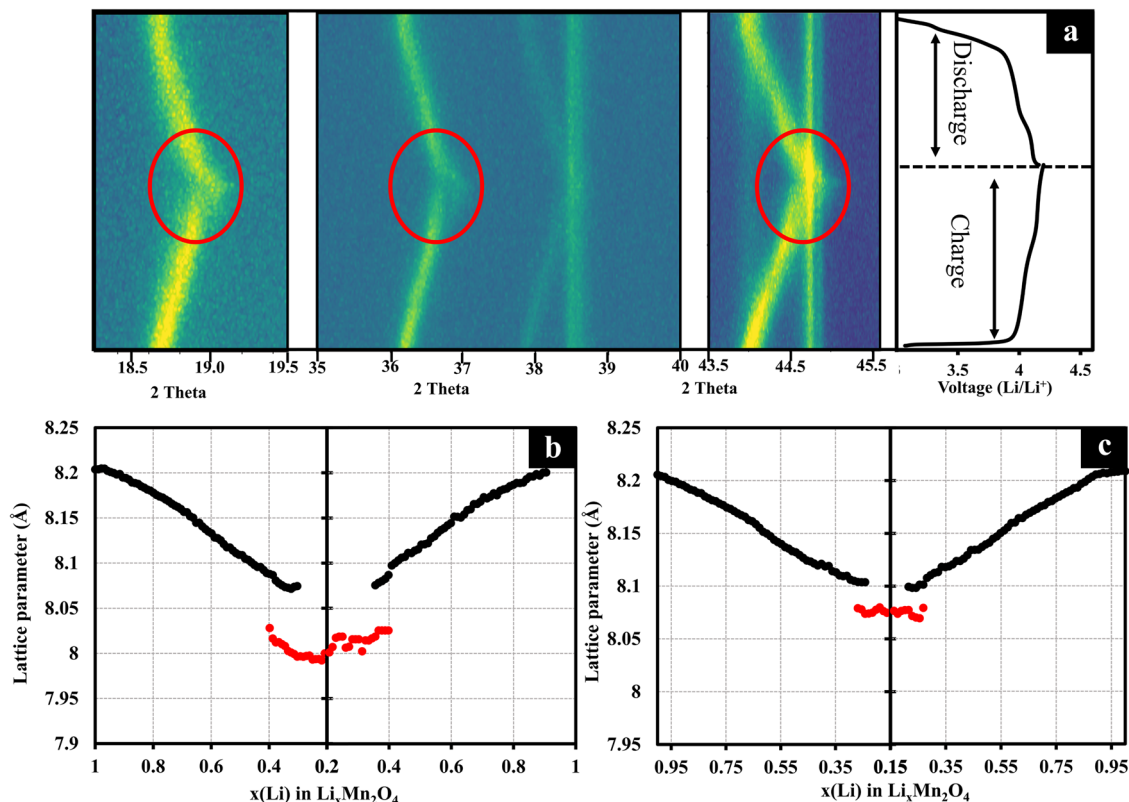


Fig. 6 Structural transition altering in lattice parameters of P-LMO and LMO@C cathodes upon lithium deintercalation/intercalation. a *In operando* XRD patterns during charging and discharging. **b–c** The correlation between lattice parameter and the amount of Li in LiMn₂O₄ in **(b)** P-LMO, and **(c)** LMO@C.

phases of LiMn₂O₄ + Li_{1-δ}Mn₂O₄ and the mixed phases with λ-MnO₂. Nevertheless, the phase between single-phase LiMn₂O₄ and the mixed phases of LiMn₂O₄ + Li_{1-δ}Mn₂O₄ is difficult to be distinguished. In contrast, the mixed phase of λ-MnO₂ can be observed from the appearance of λ-MnO₂ lattice parameter at *ca.* 8.02–8.07 Å and the presence of new phase at high angle described in the circle in Figs. S6 and 6a⁸¹.

In P-LMO (Fig. 6b), the lattice parameter continuously decreased from 8.20 Å to 8.0 Å during charging process with the existence of λ-MnO₂ phase at xLi⁺ of *ca.* 0.4–0.2 (~60% Li deintercalation). Whilst, the LMO@C (Fig. 6c) exhibits much smaller amounts of λ-MnO₂ phase, presented after Li deintercalated over *ca.* 75% (xLi⁺ = *ca.* 0.25–0.15). The smaller appearance of λ-MnO₂ phase and lower changing in lattice parameter of LMO@C indicating to the lower generation of λ-MnO₂ and suppressed contraction/expansion of the crystal lattice⁶².

To further clarify the cathode degradation, the impedance measurement with the half-cell configuration of P-LMO and LMO@C was used to consider the cathode properties and Li-ion diffusion coefficient as shown in Fig. 7. The Nyquist plots can be well-fitted with the equivalent circuit, as shown in the Fig. 7a. The T (Tangent hyperbolic) symbol corresponds to the finite space Warburg. According to Fig. 7 and Table S5, before cycling, the R_{ct} of LMO@C cell is significantly lower than that of P-LMO indicating the improvement of conductivity from carbon coated. Moreover, after cycling, the R_{ct} of P-LMO cell is rapidly increased for 86 Ω, while the R_{ct} of LMO@C is increased only 19.6 Ω. The four times lower in the impedance growth can be assumed from the decreasing Mn dissolution at the LMO@C cathode⁸⁵. The encapsulated carbon shell can reduce the direct contact between the electrolyte and the cathode reducing side reactions and the Mn dissolution.

The Li-ion diffusion coefficient was calculated from the plot between low-frequency Warburg region and Z' (Ω) by employing Eq. 11³⁷.

$$D_{Li}^+ = \frac{R^2 T^2}{2A^2 n^4 F^4 c^2 \sigma^2} \quad (11)$$

where *R* is the gas constant, *T* is the absolute temperature, *A* is the area of electrode, *n* refers to the number of electrons involved in redox reaction, *F* is Faraday's constant, *c* is the concentration of Li in active material, and *σ* is the Warburg coefficient obtained from the slope. The *D*_{Li⁺} values (Table S6) of P-LMO and LMO@C are 5.5 × 10⁻¹⁵, and 1.1 × 10⁻¹⁴, respectively. These results indicate that the carbon shell can also improve the Li ion conductivity. Note, the *D*_{Li⁺} values of LiMn₂O₄ material were widely reported in the value between the range of 10⁻¹³–10⁻¹⁵ cm²/s^{86–88}. Moreover, after 1000 cycles of stability test at 1 C, the *D*_{Li⁺} of P-LMO cell is significantly decreased to 1.1 × 10⁻¹⁵ cm²/s, while LMO@C cell exhibits high *D*_{Li⁺} of 8.1 × 10⁻¹⁵ cm²/s. This evidence clearly shows the suppression of Mn dissolution over long cycling.

Conclusions

In summary, the carbon nanoparticles were successfully coated on Mn-rich LiMn₂O₄ cathode forming the core-shell structure namely LMO@C by a scalable mechanofusion process, which is a solid-solid mixing process without using any solvent with a nearly 100% yield of production. The LMO@C exhibits superior rate-capability and cycling stability than P-LMO. The improved cycling stability can be mainly attributed to the suppression of Mn dissolution- migration-anode deposition (DMD) process which was investigated by the post-mortem analyses. Ex situ SEM/EDX, ICP-OES and ex situ XPS reveal the lower amount of

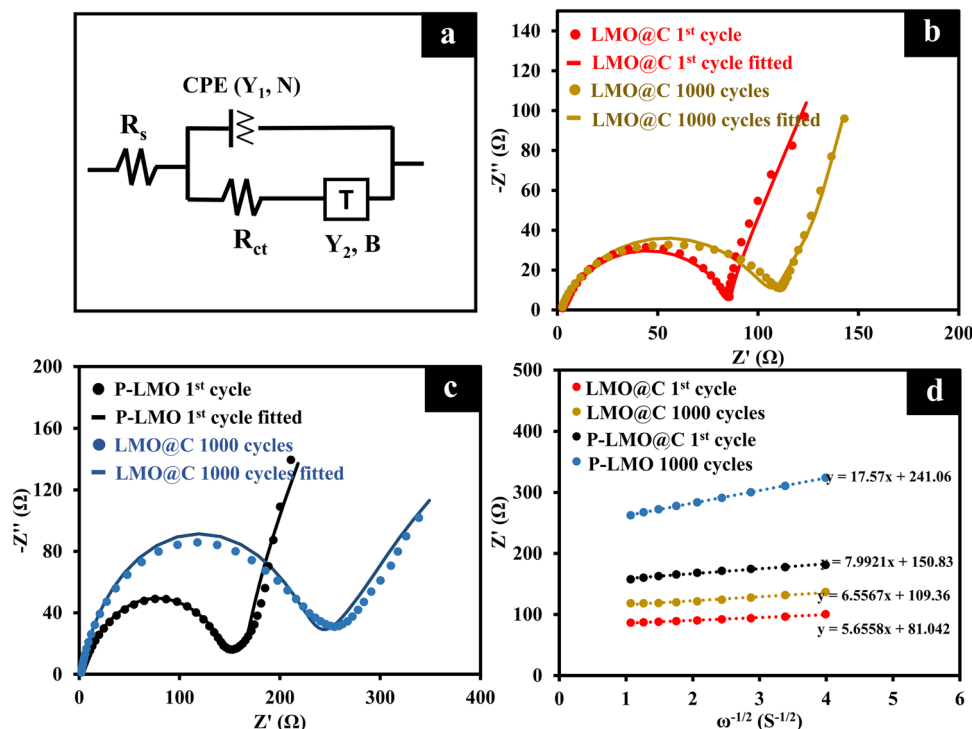


Fig. 7 Impedance measurement of half-cell P-LMO and LMO@C representing the cathode degradation after cycling. **a** The fitted equivalent circuit. **b–c** EIS curves and fitted curves in the half-cell CR2032 of **(b)** LMO@C, and **(c)** P-LMO before and after cycling. **d** The plot between Z' and $\omega^{-1/2}$ at low-frequency region for P-LMO and LMO@C.

Mn deposition on the anode surface of LMO@C with *ca.* 1.5–2 times lower than the P-LMO. The lower Mn dissolution results in a lesser extent of impedance growth and better Li^+ diffusion coefficient. Moreover, both the P-LMO and LMO@C show the generation of λ - MnO_2 mixed with $\text{Li}_{1.6}\text{Mn}_2\text{O}_4$ phases as it can be observed from the rapidly dropped in the lattice parameter when Li was deintercalated over *ca.* 70–80%. However, the LMO@C exhibits lower change in the lattice parameter compared with the P-LMO, indicating to the lower generation of λ - MnO_2 phase. Overall, the LMO@C can lessen the DMD process as well as minimize the phase transition leading to an improved cycling stability in 18,650 cylindrical batteries.

Methods

Synthesis of LMO@C core@shell materials. The carbon-coated LiMn_2O_4 with the core-shell structure (LMO@C) was synthesized by the solvent-free mechano-fusion process using NOBILTA machine (NOM-130, Hosokawa Micron Corporation, Japan). Firstly, 90 wt.% of LiMn_2O_4 was transferred to the mechano-fusion chamber and operated at 1000 rpm for 20 min. Then, the 10 wt.% of conductive carbon (Super P, TIMCAL) was added without any solvent and operated at 5000 rpm for 30 min.

Physical characterization. The morphologies of the P-LMO and the as-synthesized LMO@C were characterized by field-emission scanning electron microscopy (FESEM, JSM7001F, JEOL Ltd.) and transmission electron microscopy (TEM, JEM-ARM200F, JEOL Ltd.). The structure of materials was investigated by X-ray diffraction (XRD, Bruker, D8 Advance) using a Cu K α radiation ($\lambda = 1.54056 \text{ \AA}$). The Rietveld refinement was calculated using the Raetia software. The lattice parameters of *in operando* XRD were calculated using the TOPAS software by excluding the Bragg reflections from Al and Be windows. The element composition was explored by X-ray photoelectron spectroscopy (XPS, Kratos Axis Ultra DLD) using the monochromatic Al-K α (1486.7 eV) as the excitation source and C 1s (284.6 eV) for a reference binding energy. The amount of Mn dissolution and deposition on the anode side was obtained from an inductively coupled plasma–optical emission spectrometry (ICPOES, Agilent Technologies 700 series). Raman spectra were collected from a dispersive Raman spectrometer (SENTERRA, Bruker) with an excitation wavelength of 532 nm. Thermogravimetric analysis (TGA) was performed using STA PT1600 under an oxygen atmosphere at a

heating rate of $10 \text{ }^\circ\text{C min}^{-1}$. The electrical resistivity of electrodes was measured using a four-point probe technique (JANDLE, Model RM3000+, UK). For *in operando* XRD, the P-LMO and LMO@C specimens were prepared in the *in operando* XRD cell (LRCS, Amiens) coupled with the XRD machine (Bruker) and Autolab (PGSTAT 302 N). The XRD spectrum was collected every 7.8 min at 2 Theta of 3–80° during charging and discharging.

Coin-cell fabrication and electrochemical evaluation. The P-LMO and LMO@C electrodes were fabricated by mixing of active materials, carbon black, and PVDF in a weight ratio of 8:1:1 dissolved in NMP and sonicated for 2 h. The as-prepared slurry was coated on the Al foil with a mass loading of *ca.* 5–6 mg per a current collector area of 1.96 cm^2 . The CR2032 coin cells were fabricated using the as-prepared cathode with Li foil anode assembled in an argon-filled glove box (Mbraun labstar glove box workstation). 1.0 M LiPF_6 in EC:DEC (1:1 by volume) was used as an electrolyte. The commercial polypropylene (Celgard) was used as a separator. The electrochemical performance of batteries was tested using Galvanostatic charge-discharge (GCD, NEWARE battery tester).

Fabrication of cylindrical 18650 LIBs and electrochemical evaluation. All the fabrication processes were performed in a dry room with a dew point temperature of $-40 \text{ }^\circ\text{C}$ except for the electrolyte injection process at $-55 \text{ }^\circ\text{C}$. For the cathode slurry preparation, the P-LMO and LMO@C were prepared by mixing of active materials, carbon black, and PVDF in a weight ratio of 0.956: 0.022: 0.022 in NMP and stirred for 12 h using a vacuum planetary mixer (MTI Corp.). On the other hand, the graphite anode slurry was prepared by mixing 0.966: 0.017: 0.017 weight ratio of graphite, carbon black, and CMC/SBR in water. Next, the as-prepared slurries were coated using a roll-to-roll automatic coating machine with a built-in dryer (MTI Corp.) at $120 \text{ }^\circ\text{C}$. The thicknesses of cathode and anode were controlled at *ca.* 240 μm and 228 μm , respectively. The electrodes were processed through pressing, rolling, slitting, cutting, winding, electrolyte injection, and crimping. The EJN04 commercial LMO electrolyte (Gelon LIB) and a tri-layer PP/PE/PP were used as the electrolyte and the separator, respectively. For the capacity determination, the fabricated cells were charged to 4.2 V at 0.1 C ($C = 1400 \text{ mA}$) using CCCV and discharged to 3.0 V at 0.1 C. The rate capability test was performed using CCCV at 0.1 C, 0.25 C, 0.5 C, 0.75 C, and 1 C. Cycling test was carried out at 1 C for 900 cycles. Electrochemical Impedance Spectroscopy (EIS) was conducted by using half-cell CR2032 with an electrochemical workstation (AUTOLAB, PGSTAT302N) over a frequency range of 0.01–100 kHz with an amplitude of 10 mV.

Data availability

The data generated during this study are included in the paper and the Supplementary Information.

Received: 24 April 2021; Accepted: 25 March 2022;

Published online: 19 April 2022

References

1. Goodenough, J. B. & Kim, Y. Challenges for Rechargeable Li Batteries. *Chem. Mater.* **22**, 587–603 (2010).
2. Bao, S.-J., Liang, Y.-Y., Zhou, W.-J., He, B.-L. & Li, H.-L. Enhancement of the electrochemical properties of LiMn_2O_4 through Al^{3+} and F^- co-substitution. *J. Colloid Interfac. Sci.* **291**, 433–437 (2005).
3. Lee, S., Cho, Y., Song, H.-K., Lee, K. T. & Cho, J. Carbon-Coated Single-Crystal LiMn_2O_4 Nanoparticle Clusters as Cathode Material for High-Energy and High-Power Lithium-Ion Batteries. *Angew. Chem. Int. Ed.* **51**, 8748–8752 (2012).
4. Zhang, C. et al. Enhancing Electrochemical Performance of LiMn_2O_4 Cathode Material at Elevated Temperature by Uniform Nanosized TiO_2 Coating. *ACS Sust. Chem. Eng.* **5**, 640–647 (2017).
5. Xiao, L. et al. Enhanced electrochemical stability of Al-doped LiMn_2O_4 synthesized by a polymer-pyrolysis method. *Electrochim. Acta* **54**, 545–550 (2008).
6. Jayalakshmi, M., Mohan Rao, M. & Scholz, F. Electrochemical Behavior of Solid Lithium Manganate (LiMn_2O_4) in Aqueous Neutral Electrolyte Solutions. *Langmuir* **19**, 8403–8408 (2003).
7. Miao, Y., Hynan, P., von Jouanne, A. & Yokochi, A. Current Li-Ion Battery Technologies in Electric Vehicles and Opportunities for Advancements. *Energies* **12**, 1074 (2019).
8. Xu, G., Liu, Z., Zhang, C., Cui, G. & Chen, L. Strategies for improving the cyclability and thermo-stability of LiMn_2O_4 -based batteries at elevated temperatures. *J. Mater. Chem. A* **3**, 4092–4123 (2015).
9. Stan, A., Świerczyński, M., Stroe, D., Teodorescu, R. & Andreassen, S. J. in *2014 International Conference on Optimization of Electrical and Electronic Equipment (OPTIM)*. 713–720 <https://doi.org/10.1109/OPTIM.2014.6850936> (IEEE Press).
10. Zhang, Z., Zeng, T., Lai, Y., Jia, M. & Li, J. A comparative study of different binders and their effects on electrochemical properties of LiMn_2O_4 cathode in lithium ion batteries. *J. Power Sources* **247**, 1–8 (2014).
11. Lee, M.-J., Lee, S., Oh, P., Kim, Y. & Cho, J. High Performance LiMn_2O_4 Cathode Materials Grown with Epitaxial Layered Nanostructure for Li-Ion Batteries. *Nano Lett.* **14**, 993–999 (2014).
12. Liu, T. et al. Correlation between manganese dissolution and dynamic phase stability in spinel-based lithium-ion battery. *Nat. Commun.* **10**, 4721 (2019).
13. Thackeray, M. M. Spinel Electrodes for Lithium Batteries. *J. Am. Ceram. Soc.* **82**, 3347–3354 (1999).
14. Thackeray, M. M. Manganese oxides for lithium batteries. *Prog. Solid State Chem.* **25**, 1–71 (1997).
15. Zhu, X. et al. LiMnO_2 cathode stabilized by interfacial orbital ordering for sustainable lithium-ion batteries. *Nat. Sust.* **4**, 392–401 (2021).
16. Zhan, C., Wu, T., Lu, J. & Amine, K. Dissolution, migration, and deposition of transition metal ions in Li-ion batteries exemplified by Mn-based cathodes – a critical review. *Energy Environ. Sci.* **11**, 243–257 (2018).
17. Xia, Y., Zhou, Y. & Yoshio, M. Capacity Fading on Cycling of 4 V Li / LiMn_2O_4 Cells. *J. Electrochem. Soc.* **144**, 2593–2600 (1997).
18. Tsunekawa, H. et al. Capacity Fading of Graphite Electrodes Due to the Deposition of Manganese Ions on Them in Li-Ion Batteries. *J. Electrochem. Soc.* **149**, A1326 (2002).
19. Delacourt, C. et al. Effect of Manganese Contamination on the Solid-Electrolyte-Interphase Properties in Li-Ion Batteries. *J. Electrochem. Soc.* **160**, A1099–A1107 (2013).
20. Blyr, A., Du Pasquier, A., Amatucci, G. & Tarascon, J. M. Origin of self-discharge mechanism in LiMn_2O_4 -based Li-ion cells: a chemical and electrochemical approach. *Ionics* **3**, 321–331 (1997).
21. Tesfamhret, Y., Liu, H., Chai, Z., Berg, E. & Younesi, R. On the manganese dissolution process from LiMn_2O_4 cathode material. *ChemElectroChem* **8**, 1516–1523 (2021).
22. Lee, Y. J., Wang, F., Mukerjee, S., McBreen, J. & Grey, C. P. ^6Li and ^7Li Magic-Angle Spinning Nuclear Magnetic Resonance and In Situ X-Ray Diffraction Studies of the Charging and Discharging of $\text{Li}_x\text{Mn}_2\text{O}_4$ at 4 V. *J. Electrochem. Soc.* **147**, 803 (2000).
23. Xia, H., Luo, Z. & Xie, J. Nanostructured LiMn_2O_4 and their composites as high-performance cathodes for lithium-ion batteries. *Prog. Nat. Sci.* **22**, 572–584 (2012).
24. Illuso, A., Grageda, M. & Ushak, S. Kinetic and Thermodynamic Studies on Synthesis of Mg-Doped LiMn_2O_4 Nanoparticles. *Nanomaterials* **10**, 1409 (2020).
25. Dianat, A., Seriani, N., Bobeth, M. & Cuniberti, G. Effects of Al-doping on the properties of Li–Mn–Ni–O cathode materials for Li-ion batteries: an ab initio study. *J. Mater. Chem. A* **1**, 9273–9280 (2013).
26. Cai, Z. et al. High electrochemical stability Al-doped spinel LiMn_2O_4 cathode material for Li-ion batteries. *J. Energy Storage* **27**, 101036 (2020).
27. Teng, R. et al. Effect of cation doping on the electrochemical properties of Li_2MoO_3 as a promising cathode material for lithium-ion battery. *Ionics* **26**, 4413–4422 (2020).
28. Zhou, H.-M., Zhu, Y.-H., Li, J., Sun, W.-J. & Liu, Z.-Z. Electrochemical performance of Al_2O_3 pre-coated spinel LiMn_2O_4 . *Rare Met.* **38**, 128–135 (2019).
29. Chen, Z., Qin, Y., Amine, K. & Sun, Y. K. Role of surface coating on cathode materials for lithium-ion batteries. *J. Mater. Chem.* **20**, 7606–7612 (2010).
30. Xu, Y. et al. The preparation and role of Li_2ZrO_3 surface coating $\text{LiNi}_{0.5}\text{Co}_{0.2}\text{Mn}_{0.3}\text{O}_2$ as cathode for lithium-ion batteries. *Appl. Surf. Sci.* **361**, 150–156 (2016).
31. Jiang, Q., Liu, D., Zhang, H. & Wang, S. Plasma-Assisted Sulfur Doping of LiMn_2O_4 for High-Performance Lithium-Ion Batteries. *J. Phys. Chem. C* **119**, 28776–28782 (2015).
32. Prabaharan, S. R. S., Michael, S. S. & Julien, C. Synthesis and electrochemistry of LiMn_2O_4 prepared using succinic acid as complexing agent. *Int. J. Inorg. Mater.* **1**, 21–27 (1999).
33. Velásquez, E. A. et al. Understanding the loss of electrochemical activity of nanosized LiMn_2O_4 particles: a combined experimental and ab initio DFT study. *J. Mater. Chem. A* **6**, 14967–14974 (2018).
34. Sun, W. et al. Hierarchical donut-shaped LiMn_2O_4 as an advanced cathode material for lithium-ion batteries with excellent rate capability and long cycle life. *J. Mater. Chem. A* **3**, 8165–8170 (2015).
35. Jayaraman, S. et al. Synthesis of porous LiMn_2O_4 hollow nanofibers by electrospinning with extraordinary lithium storage properties. *Chem. Commun.* **49**, 6677–6679 (2013).
36. Wang, H.-Q. et al. Excellent stability of spinel LiMn_2O_4 -based cathode materials for lithium-ion batteries. *Electrochim. Acta* **177**, 290–297 (2015).
37. Selvamani, V., Phattharasupakun, N., Wutthiprom, J. & Sawangphruk, M. High-performance spinel LiMn_2O_4 @carbon core-shell cathode materials for Li-ion batteries. *Sustain. Energy Fuels* **3**, 1988–1994 (2019).
38. Phattharasupakun, N. et al. Core-shell Ni-rich NMC-Nanocarbon cathode from scalable solvent-free mechanofusion for high-performance 18650 Li-ion batteries. *Energy Storage Mater.* **36**, 485–495 (2021).
39. Long, D. H. et al. Coating Lithium Titanate with Nitrogen-Doped Carbon by Simple Refluxing for High-Power Lithium-Ion Batteries. *ACS Appl. Mater. Interfac.* **7**, 10250–10257 (2015).
40. Ilango, P. R., Prasanna, K., Do, S. J., Jo, Y. N. & Lee, C. W. Eco-friendly nitrogen-containing carbon encapsulated LiMn_2O_4 cathodes to enhance the electrochemical properties in rechargeable Li-ion batteries. *Sci. Rep.* **6**, 29826 (2016).
41. Zheng, L., Wei, C., Garayt, M. D. L., MacInnis, J. & Obrovac, M. N. Spherically Smooth Cathode Particles by Mechanofusion Processing. *J. Electrochem. Soc.* **166**, A2924–A2927 (2019).
42. Vadivel, S., Phattharasupakun, N., Wutthiprom, J., duangdangchote, S. & Sawangphruk, M. High-Performance Li-Ion Batteries Using Nickel-Rich Lithium Nickel Cobalt Aluminium Oxide–Nanocarbon Core–Shell Cathode: In Operando X-ray Diffraction. *ACS Appl. Mater. Interfac.* **11**, 30719–30727 (2019).
43. Kim, C. S. et al. Facile dry synthesis of sulfur-LiFePO₄ core-shell composite for the scalable fabrication of lithium/sulfur batteries. *Electrochem. Commun.* **32**, 35–38 (2013).
44. Bhandari, A. & Bhattacharya, J. Review—Manganese Dissolution from Spinel Cathode: Few Unanswered Questions. *J. Electrochem. Soc.* **164**, A106–A127 (2016).
45. Abbas, S. M. et al. Ag-Modified LiMn_2O_4 Cathode for Lithium-Ion Batteries: coating functionalization. *Energies* **13**, 5194 (2020).
46. Jiang, Q., Wang, X. & Tang, Z. Improving the Electrochemical Performance of LiMn_2O_4 by Amorphous Carbon Coating. *Fuller. Nanotub. Carbon Nanostruct.* **23**, 676–679 (2015).
47. Riippi, M., Tanninen, V.-P. & Yliruusi, J. Effect of compression force on the crystal properties of erythromycin acistrate tablets. *Eur. J. Pharm. Biopharm.* **50**, 365–371 (2000).
48. Pirttimäki, J., Laine, E., Ketolainen, J. & Paronen, P. Effects of grinding and compression on crystal structure of anhydrous caffeine. *Int. J. Pharm.* **95**, 93–99 (1993).
49. Slautin, B. et al. Local Study of Lithiation and Degradation Paths in LiMn_2O_4 Battery Cathodes: confocal raman microscopy approach. *Batteries* **4**, 21 (2018).

50. Ramana, C. V., Massot, M. & Julien, C. M. XPS and Raman spectroscopic characterization of LiMn_2O_4 spinels. *Surf. Interfac. Anal.* **37**, 412–416 (2005).
51. Baddour-Hadjean, R. & Pereira-Ramos, J.-P. Raman Microspectrometry Applied to the Study of Electrode Materials for Lithium Batteries. *Chem. Rev.* **110**, 1278–1319 (2010).
52. Ammundsen, B., Burns, G. R., Islam, M. S., Kanoh, H. & Rozière, J. Lattice Dynamics and Vibrational Spectra of Lithium Manganese Oxides: A Computer Simulation and Spectroscopic Study. *J. Phys. Chem. B* **103**, 5175–5180 (1999).
53. Zhao, S., Bai, Y., Chang, Q., Yang, Y. & Zhang, W. Surface modification of spinel LiMn_2O_4 with FeF_3 for lithium ion batteries. *Electrochim. Acta* **108**, 727–735 (2013).
54. Zhuo, H. et al. Improved electrochemical performance of spinel LiMn_2O_4 in situ coated with graphene-like membrane. *J. Power Sources* **247**, 721–728 (2014).
55. Gieu, J.-B. et al. New insights into the characterization of the electrode/electrolyte interfaces within $\text{LiMn}_2\text{O}_4/\text{Li}_4\text{Ti}_5\text{O}_{12}$ cells, by X-ray photoelectron spectroscopy, scanning Auger microscopy and time-of-flight secondary ion mass spectrometry. *J. Mater. Chem. A* **5**, 15315–15325 (2017).
56. Gauthier, N., Courrèges, C., Demeaux, J., Tessier, C. & Martinez, H. Probing the in-depth distribution of organic/inorganic molecular species within the SEI of LTO/NMC and LTO/LMO batteries: A complementary ToF-SIMS and XPS study. *Appl. Surf. Sci.* **501**, 144266 (2020).
57. Edström, K., Gustafsson, T. & Thomas, J. O. The cathode–electrolyte interface in the Li-ion battery. *Electrochim. Acta* **50**, 397–403 (2004).
58. Nordh, T. et al. Manganese in the SEI Layer of $\text{Li}_4\text{Ti}_5\text{O}_{12}$ Studied by Combined NEXAFS and HAXPES Techniques. *J. Phys. Chem. C* **120**, 3206–3213 (2016).
59. Eriksson, T. et al. Surface Analysis of LiMn_2O_4 Electrodes in Carbonate-Based Electrolytes. *J. Electrochem. Soc.* **149**, A69 (2002).
60. Ben, L. et al. Unusual Spinel-to-Layered Transformation in LiMn_2O_4 Cathode Explained by Electrochemical and Thermal Stability Investigation. *ACS Appl. Mater. Interfac.* **9**, 35463–35475 (2017).
61. Delluva, A. A., Dudoff, J., Teeter, G. & Holewinski, A. Cathode Interface Compatibility of Amorphous LiMn_2O_4 (LMO) and $\text{Li}_7\text{La}_3\text{Zr}_2\text{O}_{12}$ (LLZO) Characterized with Thin-Film Solid-State Electrochemical Cells. *ACS Appl. Mater. Interfac.* **12**, 24992–24999 (2020).
62. Tang, X. et al. Investigation of the self-discharge behaviors of the LiMn_2O_4 cathode at elevated temperatures: in situ X-ray diffraction analysis and a co-doping mitigation strategy. *J. Mater. Chem. A* **7**, 13364–13371 (2019).
63. Tang, D. et al. Surface Structure Evolution of LiMn_2O_4 Cathode Material upon Charge/Discharge. *Chem. Mater.* **26**, 3535–3543 (2014).
64. Wu, X. M., Chen, S., Ma, M. Y. & Liu, J. B. Synthesis of Co-coated lithium manganese oxide and its characterization as cathode for lithium ion battery. *Ionics* **17**, 35–39 (2011).
65. Li, A., Shao, Z., Yang, S., Li, X. & Zhang, A. Precipitation synthesis and enhanced electrochemical performance of graphene-modified LiMn_2O_4 for lithium-ion batteries. *Ionics* **26**, 3231–3238 (2020).
66. Lee, H.-W. et al. Ultrathin Spinel LiMn_2O_4 Nanowires as High Power Cathode Materials for Li-Ion Batteries. *Nano Lett.* **10**, 3852–3856 (2010).
67. Ilango, P. R., Prasanna, K., Subburaj, T., Jo, Y. N. & Lee, C. W. Facile longitudinal unzipping of carbon nanotubes to graphene nanoribbons and their effects on LiMn_2O_4 cathodes in rechargeable lithium-ion batteries. *Acta Mater.* **100**, 11–18 (2015).
68. Shen, C. et al. Facile One-Step Dynamic Hydrothermal Synthesis of Spinel LiMn_2O_4 /Carbon Nanotubes Composite as Cathode Material for Lithium-Ion Batteries. *Materials* **12**, 4123 (2019).
69. Lung-Hao Hu, B., Wu, F.-Y., Lin, C.-T., Khlobystov, A. N. & Li, L.-J. Graphene-modified LiFePO_4 cathode for lithium ion battery beyond theoretical capacity. *Nat. Commun.* **4**, 1687 (2013).
70. Sun, L., Wang, J. & Bonaccorso, E. Conductivity of individual particles measured by a microscopic four-point-probe method. *Sci. Rep.* **3**, 1991–1991 (2013).
71. Park, M., Zhang, X., Chung, M., Less, G. B. & Sastry, A. M. A review of conduction phenomena in Li-ion batteries. *J. Power Sources* **195**, 7904–7929 (2010).
72. Li, H. et al. Effects of Mg doping on the remarkably enhanced electrochemical performance of $\text{Na}_3\text{V}_2(\text{PO}_4)_3$ cathode materials for sodium ion batteries. *J. Mater. Chem. A* **3**, 9578–9586 (2015).
73. Xia, J. et al. Comparative Study on Methylene Methyl Disulfonate (MMDs) and 1,3-Propane Sultone (PS) as Electrolyte Additives for Li-Ion Batteries. *J. Electrochem. Soc.* **161**, A547–A553 (2014).
74. Xia, J. et al. Study of Methylene Methanedisulfonate as an Additive for Li-Ion Cells. *J. Electrochem. Soc.* **161**, A84–A88 (2013).
75. Jo, J. et al. One-pot pyro synthesis of a nanosized- $\text{LiMn}_2\text{O}_4/\text{C}$ cathode with enhanced lithium storage properties. *RSC Adv.* **9**, 24030–24038 (2019).
76. Shin, H., Park, J., Sastry, A. M. & Lu, W. Effects of Fluoroethylene Carbonate (FEC) on Anode and Cathode Interfaces at Elevated Temperatures. *J. Electrochem. Soc.* **162**, A1683–A1692 (2015).
77. Komaba, S. et al. Impact of 2-Vinylpyridine as Electrolyte Additive on Surface and Electrochemistry of Graphite for CLiMn_2O_4 Li-Ion Cells. *J. Electrochem. Soc.* **152**, A937 (2005).
78. Komaba, S., Kumagai, N. & Kataoka, Y. Influence of manganese(II), cobalt(II), and nickel(II) additives in electrolyte on performance of graphite anode for lithium-ion batteries. *Electrochim. Acta* **47**, 1229–1239 (2002).
79. Amine, K. et al. Improved lithium manganese oxide spinel/graphite Li-ion cells for high-power applications. *J. Power Sources* **129**, 14–19 (2004).
80. Zhan, C. et al. Mn(II) deposition on anodes and its effects on capacity fade in spinel lithium manganate–carbon systems. *Nat. Commun.* **4**, 2437 (2013).
81. Paulsen, J. M. & Dahn, J. R. Phase Diagram of Li–Mn–O Spinel in Air. *Chem. Mater.* **11**, 3065–3079 (1999).
82. Han, S. C. et al. Gadolinium-Doped LiMn_2O_4 Cathodes in Li Ion Batteries: understanding the Stabilized Structure and Enhanced Electrochemical Kinetics. *J. Electrochem. Soc.* **159**, A1867–A1873 (2012).
83. Song, B. et al. Metastable $\text{Li}_{1+\delta}\text{Mn}_2\text{O}_4$ ($0 \leq \delta \leq 1$) Spinel Phases Revealed by in Operando Neutron Diffraction and First-Principles Calculations. *Chem. Mater.* **31**, 124–134 (2019).
84. Julien, C. M., Mauger, A., Zaghbi, K. & Groult, H. Comparative Issues of Cathode Materials for Li-Ion Batteries. *Inorganics* **2**, 132–154 (2014).
85. Jang, D. H., Shin, Y. J. & Oh, S. M. Dissolution of Spinel Oxides and Capacity Losses in 4V $\text{Li}/\text{Li}_x\text{Mn}_2\text{O}_4$ Cells. *J. Electrochem. Soc.* **143**, 2204–2211 (1996).
86. Liu, Q. et al. Facile flameless combustion synthesis of high-performance boron-doped LiMn_2O_4 cathode with a truncated octahedra. *J. Alloy. Compd.* **874**, 159912 (2021).
87. Marincas, A.-H. & Ilea, P. Enhancing Lithium Manganese Oxide Electrochemical Behavior by Doping and Surface Modifications. *Coatings* **11**, 456 (2021).
88. Sarkar, T., Prakasha, K. R., Bharadwaj, M. D. & Prakash, A. S. Lithium diffusion study in Li_2MnO_3 and $\text{Li}_{1.17}\text{Ni}_{0.17}\text{Mn}_{0.67}\text{O}_2$: A combined experimental and computational approach. *Phys. Chem. Chem. Phys.* **19**, 31724–31730 (2017).

Acknowledgements

This work was financially supported under Program Management Unit for National Competitiveness Enhancement (PMU-C) by Office of National Higher Education Science Research and Innovation Policy Council (NXPO) and Thailand Science Research and Innovation (TSRI) (153655) and under the Fundamental Fund by TSRI and VISTEC (161543) and as well as Energy Policy and Planning Office (EPPO), Ministry of Energy, Thailand. In addition, this work was supported by FRC, VISTEC.

Author contributions

C.T.: Writing—original draft, Formal analysis, Data curation, Investigation, Methodology, Visualization. S.S.: Methodology, Investigation, Formal analysis. N.P.: Methodology, Investigation, Formal analysis. S.D.: Methodology, Investigation, Formal analysis. P.C.: Methodology, Investigation, Formal analysis. N.J.: Methodology, Investigation, Formal analysis. P.B.: Methodology, Investigation, Formal analysis. M.S.: Funding acquisition, Supervision, Investigation, Resources, Writing—review & editing, Conceptualization, Formal analysis.

Competing interests

The authors declare no competing interests.

Additional information

Supplementary information The online version contains supplementary material available at <https://doi.org/10.1038/s42004-022-00670-y>.

Correspondence and requests for materials should be addressed to Montree Sawangphruk.

Peer review information *Communications Chemistry* thanks the anonymous reviewers for their contribution to the peer review of this work.

Reprints and permission information is available at <http://www.nature.com/reprints>

Publisher's note Springer Nature remains neutral with regard to jurisdictional claims in published maps and institutional affiliations.



Open Access This article is licensed under a Creative Commons Attribution 4.0 International License, which permits use, sharing, adaptation, distribution and reproduction in any medium or format, as long as you give appropriate credit to the original author(s) and the source, provide a link to the Creative Commons license, and indicate if changes were made. The images or other third party material in this article are included in the article's Creative Commons license, unless indicated otherwise in a credit line to the material. If material is not included in the article's Creative Commons license and your intended use is not permitted by statutory regulation or exceeds the permitted use, you will need to obtain permission directly from the copyright holder. To view a copy of this license, visit <http://creativecommons.org/licenses/by/4.0/>.

© The Author(s) 2022